Rodriguez-Millan, M., Garcia-Gonzalez, D., Rusinek, A., Abed, F. & Arias, A. (2018). Perforation mechanics of 2024 aluminium protective plates subjected to impact by different nose shapes of projectiles. *Thin-Walled Structures*, vol. 123, pp. 1-10.

DOI: 10.1016/j.tws.2017.11.004

Perforation mechanics of 2024 aluminium protective plates subjected to impact by different nose shapes of projectiles

M. Rodriguez-Millan[a]*, D. Garcia-Gonzalez[b,c], A. Rusinek[d], F.Abed[e], A.Arias[b]

[a] *Department of Mechanical Engineering, University Carlos III of Madrid, Avda. de la Universidad 30, 28911 Leganés, Madrid, Spain*

[b] *Department of Continuum Mechanics and Structural Analysis, University Carlos III of Madrid, Avda. de la Universidad 30, 28911 Leganés, Madrid, Spain*

[c] *Department of Engineering Science, University of Oxford, Parks Road, Oxford OXI 3PJ, UK*

[d] *Laboratory of Microstructure Studies and Mechanics of Materials (LEM3), Lorraine University, 1 route dArs Laquenexy, 57078 Metz Cedex 3, France*

[e] *Department of Civil Engineering, American University of Sharjah, P.O. Box 26666 Sharjah, U.A.E.*

* *corresponding author*

Email address: mrmillan@ing.uc3m.es*(M.Rodríguez-Millán)*

Phone number: +34916245860

ABSTRACT:

This paper focuses on the mechanical behaviour of aluminium alloy 2024-T351 under impact loading. This study has been carried out combining experimental and numerical techniques. Firstly, experimental impact tests were conducted on plates of 4 mm of thickness covering impact velocities from 50 m/s to 200 m/s and varying the stress state through the projectile nose shape: conical, hemispherical and blunt. The mechanisms behind the perforation process were studied depending on the projectile configuration used by analyzing the associated failure modes and post-mortem deflection. Secondly, a numerical study of the mechanical behaviour of aluminium alloy 2024-T351 under impact loading was conducted. To this end, a three-dimensional model was developed in the finite element solver ABAQUS/Explicit. This model combines Lagrangian elements with Smoothed Particle Hydrodynamics (SPH) elements. A good correlation was obtained between numerical and experimental results in terms of residual and ballistic limit velocities.

KEYWORDS:

AA 2024-T351 · Perforation · Ballistic limit · Energy absorption · FEM-SPH

Highlights

- The ballistic limit for different projectile shapes has been determined.
- Different failure modes have been observed depending on the stress state associated to projectile shape.
- Local effects were more important for conical and hemispherical nose projectiles.
- A 3D numerical model has been used to simulate the impact tests on plates.
- Good agreement has been found between experiments and FE simulations.

1. Introduction

The impact-protective capacity of structural components has become a relevant requirement for the automotive and aerospace industries. Both energy absorption and crashworthiness concepts are essential for the development of new vehicles and aircraft. In such applications, design challenges are focused on structural crashworthiness and light-weight vehicles. Accordingly, research on crashworthiness has managed to considerably reduce fatalities by 26% in the USA from 2005 to 2011 [1].

Several studies have been carried out to study the impact behaviour of metallic plates. In this field, the research developed by Borvik and co-authors [2-4] and Gupta and co-authors [5-6] can be highlighted because of their relevance. Their work focused on mechanical variables that govern the penetration process, such as the target material, target dimensions, projectile nose shape and impact velocity. In this regard, the projectile-nose determines the stress state and its effect varies with several parameters such as the thickness of the target plate, impact velocity, target thickness to projectile diameter ratio and nose angle or nose radius of the projectiles [7-12]. However, there still remains a need for a systematic study of the influence of projectile nose shape on global deformations (plate deflection, bending and membrane stretching) and local deformations (ductile hole formation, petalling, plugging, rear bulging, discing, tensile tearing, thinning, shear banding and necking) of aluminium plates under impact loading. The study of energy absorption capacity on metallic plates can provide relevant information on the effects of local impacts on the global structural response. This work focuses on the perforation process of a ductile plate of AA2024-T3 when it is subjected to an impact of a non-deformable projectile. To the authors' knowledge, none of the previous impact and perforation studies of AA2024-T3 investigated the effect of the projectile shape on the material response, while keeping the same kinetic energy and boundary conditions. The new experimental data of residual velocities for AA2024-T3 presented in this study can be very useful and relevant especially for the design and optimization of protective structures.

Finite Element Method (FEM) has been commonly used to simulate impact problems. This method provides models that predict residual velocities, ballistic limits and failure mechanisms depending on the projectile-target configurations [13-18]. Most of the previous studies did not focus on quantifying the amount of global and local energy absorption during the impact process. A common problem in FEM is the excessive element distortions encountered in dynamic loading simulations [19]. Element deletion approach could be used to erode highly distorted elements but presents inconsistencies and no physical fundamentals [20]. In order to minimize this problem, several authors [21-22] described the advantage of using adaptive meshing algorithm as an alternative technique for the analysis of plate-impact events. The scheme of the adaptive mesh available in some commercial FE software (e.g., ABAQUS [23]) combines the features of Lagrangian and Eulerian analyses which allows for obtaining a high mesh quality during the whole simulation. However, the adaptive remeshing technique is computationally expensive and can lead to numerical instabilities and unexpected termination of the simulation [24]. A mesh-free Smoothed Particle Hydrodynamics (SPH) technique presents several advantages over conventional FEM and can be also used for impact problems [25]. This avoids extreme mesh distortions in problems that involve impact and penetration. However, SPH technique encounters several difficulties in engineering problems such as tensile instability; difficulty in loading essential boundary condition and high computational cost. A new computational method has been

recently proposed to fill the gap between conventional FEM and models based on SPH. This method is based on a Lagragian mesh whose elements are converted into SPH elements when a *conversion variable* (strain, stress or any state variable) reaches a critical value. By this way, some distortion- and instability-related problems are avoided without introducing a too expensive computational cost. This approach assumes a rigid coupling between SPH particles and Lagrangian nodes at the interface zone [22;25-27]. The rigid interface definition, however, induces some problems, particularly at highly localized regions as discussed in detail by Zhang and co-authors [26]. This novel approach has been used to simulate high velocity impact computations [28], and is employed in this work for the numerical analysis. In addition to the advantages mentioned above, this method allows also for retaining the mass and mechanical properties of the elements converted into SPH particles.

The main objective of this research is the analysis of failure mechanisms of aluminium alloy 2024-T531 plates perforated by rigid projectiles of different nose shapes. Perforation tests were conducted using conical, hemispherical and blunt projectiles covering impact velocities from 50 m/s to 200 m/s. The experimental arrangement enables the determination of the impact velocity, the residual velocity and the failure mode of the aluminium plates. The experimental results were used to validate and identify the value of the mechanical variable that controls the conversion FEM- SPH method. Once the numerical model was validated with experimental data, it was used to analyse energy absorption mechanisms associated with the deformation and failure of the aluminium plates. In addition, both experimental and numerical techniques allowed for investigating the influence of impact velocity, target thickness and projectile nose shape on the failure mechanisms. The outcomes of this work provide new insights into the energy absorption and failure mechanisms behind the perforation process of AA2024 which allow for a better comprehension of its mechanical response under different impact conditions. The results presented herein provide new relevant information for the design of structures potentially subjected to impact loading such as aeronautical components.

2. Experimental Program

2.1 Material

In the present investigation, the attention is focused on the mechanical behaviour of aluminium alloy (AA) 2024-T351. The principal applications of this material are aircraft structural components, wing tension members, hardware, truck wheels, scientific instruments, veterinary and orthopaedic braces and equipment, and in rivets because of its high strength, excellent fatigue resistance and good strength-to-weight ratio. The AA 2024 T-351 has been widely studied in terms of mechanical behaviour as well as ductile failure (see a previous work of Rodríguez-Millán and co-authors [29]), but its mechanical behaviour against impact loading has not been analyzed enough. Prior to conducting the impact tests, some experiments were conducted under quasi-static conditions in order to verify the material used and its similarities with the one employed in previous published studies (see Appendix A).

2.2 Test set-up

Perforation tests were conducted using a pneumatic gas gun to launch a projectile onto an AA 2024-T351 plate specimen, see Figure 1. The maximum velocity of the projectile, denoted as *impact velocity Vo*, is reached at the end of the tube C. Both initial impact and residual velocities of the projectiles were measured during the impact tests using laser sensors attached to photodiodes and timers at D and F. The maximum error on the velocity measurements between the two sensors was estimated around $\Delta\bar{V} \approx 1\ m/s$. Further details of the experimental setup are provided in previous works [10;12]. In addition, the set-up E may be instrumented to measure the force impact or force perforation on time as reported in [40] using four piezoelectric sensors with a maximum force of 80 kN.

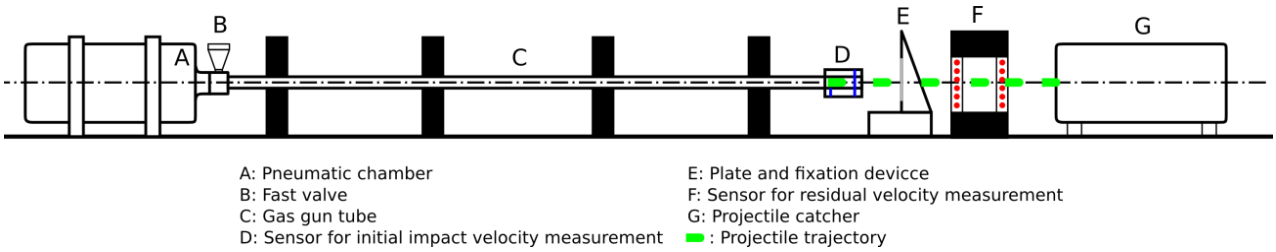

Fig. 1: Scheme of experimental set up used for perforation test.

The AA 2024-T351 specimens were clamped along four edges using a rigid support in order to reduce sliding effects during the test. This arrangement (screwing + clamping) has been discussed in previous works by the authors [10-11]. The active target area of the specimens was reduced to $100\ mm \times 100\ mm$ with a plate thickness of 4 mm, see Figure 2.

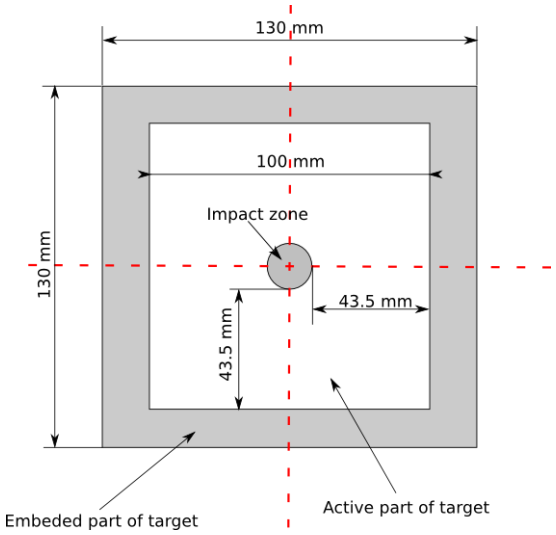

Fig. 2: Geometry and dimensions of target.

The tests were conducted using three types of projectiles released at different impact velocities up to $V_0 \approx 200\ m/s$: The projectiles were made of a maraging steel with a heat treatment to reach a yield stress close to $\bar{\sigma}_y = 2\ GPa$. The projectiles, independently of the nose shape configuration, present a maximum diameter $\phi_{projectiles} = 13\ mm$ and a constant mass of $M_p \approx 30\ g$. Their geometries and dimensions are shown in Figure 3-a-c.

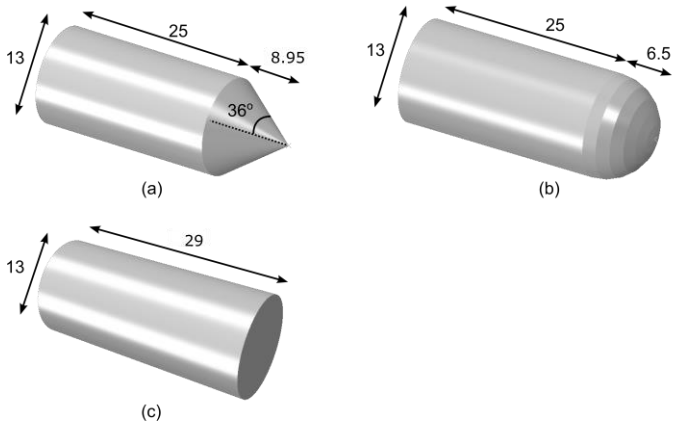

Fig. 3: Geometry and dimensions (mm) of the projectiles used in the perforation test: a) conical projectile; b) hemispherical projectile; and c) blunt projectile.

The diameter of the projectiles was approximately equal to the diameter of the barrel to ensure a perpendicular impact on the aluminium plate.

2.3 Experimental results

2.3.1 Residual velocity

Figure 4 shows the residual velocity versus impact velocity ($V_r - V_0$) curves for the three different projectile-shapes considered. The ballistic limits (V_{bl}) were found to be $147.0\ m/s$, $148.8\ m/s$ and $150.6\ m/s$ respectively for hemispherical nose, conical nose and blunt nose. This sequence of ballistic limits differs from previous results conducted on aluminium alloys AA 6082-T6 and AA 5754-H111 (reported by Rodríguez-Millán and co-authors [12]).

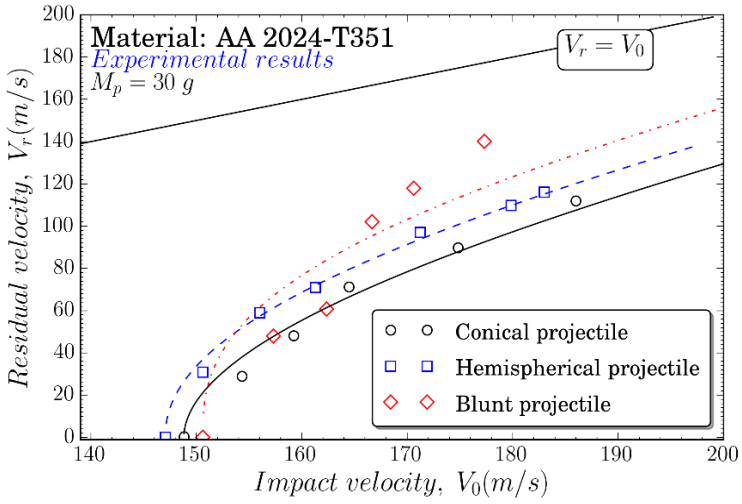

Fig. 4: Comparison of residual velocity V_r versus impact velocity V_0 between conical, hemispherical and blunt projectiles.

The results shown in Figure 5 have been fitted via the expression proposed by Recht and Ipson [31] as follows:

$$V_r = (V_0^{\kappa} - V_{bl}^{\kappa})^{1/\kappa} \quad (1)$$

where κ is a fitting parameter depending on the projectile shape that describes the trend of the relationship, determined as $\kappa = 1.92$ for the conical projectile; $\kappa = 2.13$ for the hemispherical projectile; and $\kappa = 2.61$ for the blunt projectile.

Figure 5 illustrates the amount of energy absorbed by the target versus impact velocity V_0 for the three projectile nose shapes considered. The energy absorbed by the plate, E_a, was calculated using the following expression:

$$E_a = \frac{1}{2} \cdot M_p \cdot \left(V_0^2 - V_{bl}^2\right) \quad (2)$$

The energy absorbed by the target is almost independent on the initial velocity when the plate is impacted by conical projectiles (within the range of velocities tested), see Figure 5. The same behaviour was observed in a previous work for other two aluminium alloys: AA 5754-H111 and AA 6082-T6 [12]. For the case of hemispherical projectiles, a slight variation in energy absorption with impact velocities can be noticed. In contrast, energy absorption sharply decreases as the impact velocity increases when the blunt projectile is used, see Figure 5.

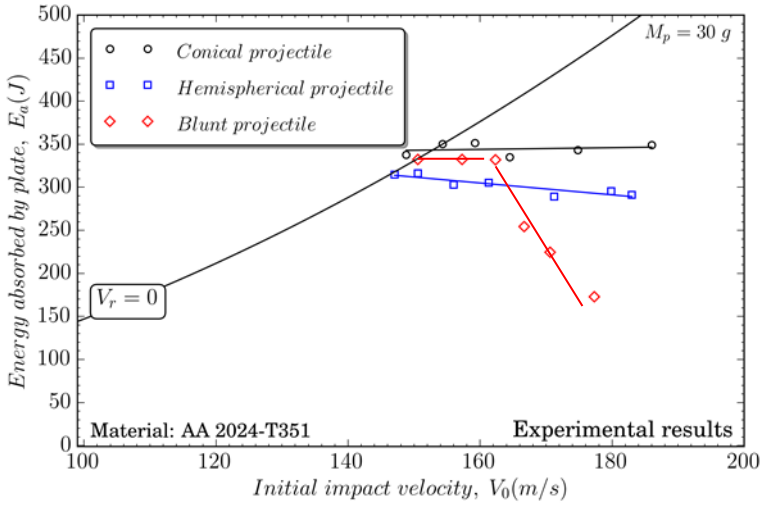

Fig. 5: Energy absorbed by the target E_a versus impact velocity V_0 for conical, hemispherical and blunt projectiles.

The different perforation mechanisms associated with the three nose-shaped projectiles considered explain the intersection shown in the $V_r - V_0$ curves (Figure 4) and in the $E_a - V_0$ curves (Figure 5). The larger ballistic limit of the blunt projectile is attributed to high yield stress of the AA 2024-T351, which enhances the critical impact velocity required for the shear bands formation. However, once the ballistic limit is exceeded, the energy consumed by this failure mechanism considerably decreases with impact velocity.

2.3.2 Failure mode

The variation in energy absorption capacity with different projectile nose shapes can be related to the corresponding difference in deformation and failure modes as shown in Figure 6. In this regard, Kpenyigba and co-authors [11] observed that the failure strain depends on the stress state induced by the projectile shape.

When using conical projectiles in the range of impact velocities considered, the failure process occurs following petalling mechanisms, see Figure 6a. Four petals were observed in these tests, what has been frequently reported for metals [12; 33-33]. Hemispherical projectiles, in contrast, led to a plate failure based on ductile hole enlargement, where the material in front of the projectile is pushed forward, see Figure 6b. Localised rear bulging with radial cracks and short petals was also observed. The plug ejected shows a diameter similar to the projectile; however, the diameter of the perforated hole was found to be smaller than the projectile's due to elastic recovery (*spring back behaviour*). For the case of blunt projectile (Figure 6c), the failure mode of the plate was dominated by shear banding leading to the ejection of a circular plug at the final stage of the perforation. This circular plug presented a diameter equal to the projectile diameter.

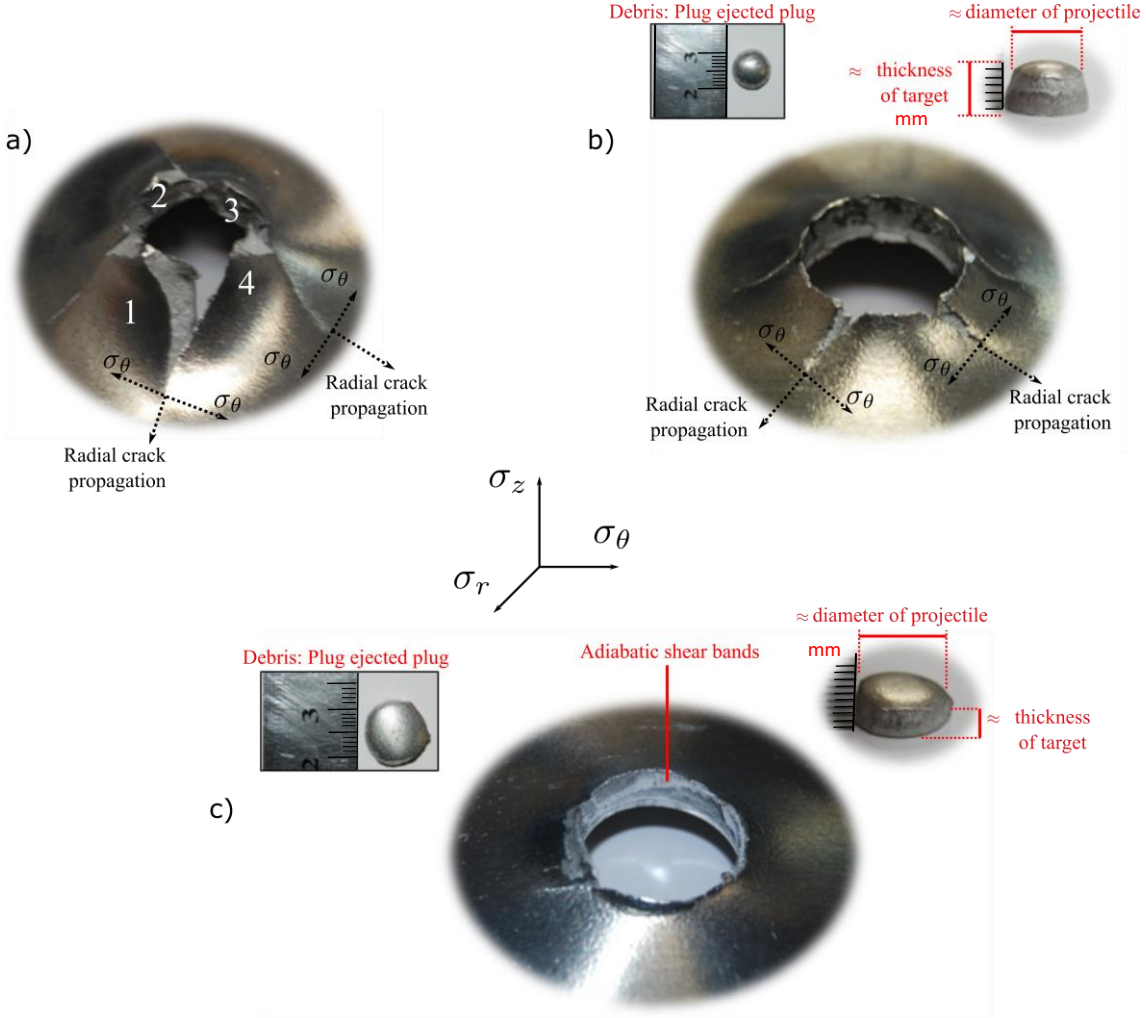

Fig. 6: Failure modes of the perforation process for the different projectiles: *a*) conical projectile, V=175 m/s; *b*) hemispherical projectile, V=171 m/s; and *c*) blunt projectile, v=168 m/s.

The cross sections have been digitalized in order to analyze the global deformation. Figure 7 shows cross sections of plates at velocities close to the ballistic limit for the three different projectile nose-shapes. For the same impact velocity, the global deformation (bending and membrane stretching) was higher when using the conical projectile configuration than for the other two configurations. However, in the case of the blunt projectile configuration, the local failure mechanisms were more energy consuming.

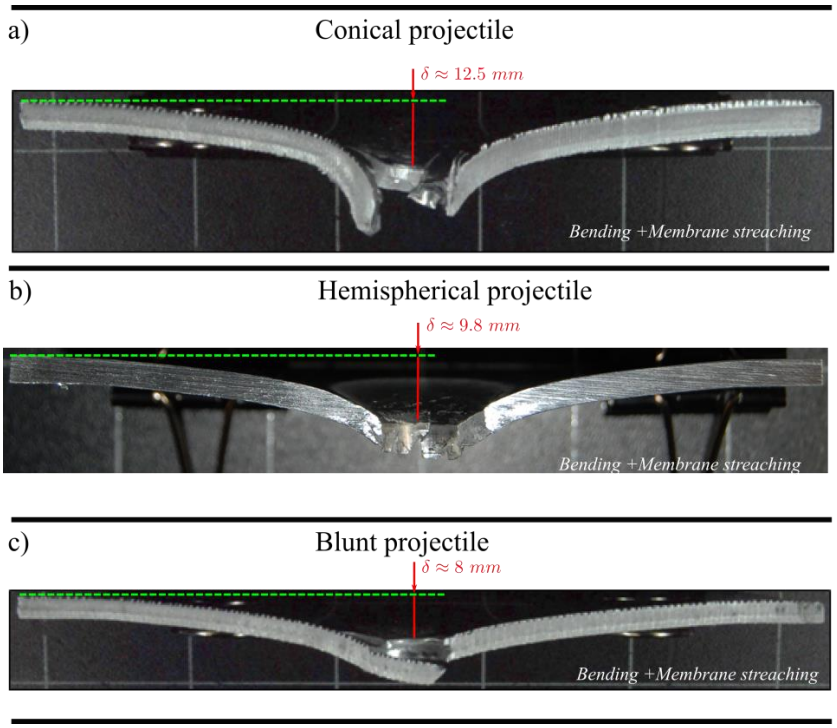

Fig. 7: Cross sections of penetrated plates by: *a*) conical projectile, V=149 m/s; *b*) hemispherical projectile, V=147 m/s; and *c*) blunt projectile, V=151 m/s.

In order to carry out a more extensive analysis of the problem, a numerical model is developed in next section providing more information about the deformation and failure processes.

3. Numerical simulations

3.1 Thermoviscoplastic material behaviour

Although some authors have observed an anisotropic behaviour in AA 2024-T351 [34-35], its mechanical behaviour is commonly defined by isotropic material models and von Mises yield function [7,36]. Since the main objective of this work is to analyse the influence of triaxiality on the energy absorption capability and how it affects the failure mechanisms that govern the perforation process, the isotropic material definition adopted has been considered. In this regard, the thermoviscoplastic

material behaviour of AA 2024-T351 plates is defined by the Johnson-Cook (JC) model [37]. This hardening law defines the effective flow stress following the expression bellow, Eq. (3). The first term of Eq. (3) defines the strain hardening due to plastic deformation ($\bar{\varepsilon}^p$) depending on the reference yield stress *A* and the material constants *B* and *n*. The second term accounts for strain rate sensitivity ($\dot{\bar{\varepsilon}}^p$) through the material parameter C and the reference strain rate $\dot{\bar{\varepsilon}}_0$. Regarding the third term, it captures the thermal softening on the material by the thermal sensitivity parameter *m*.

$$\bar{\sigma}(\bar{\varepsilon}^p, \dot{\bar{\varepsilon}}^p, T) = [A + B(\bar{\varepsilon}^p)^n]\left[1 + C \ln\left(\frac{\dot{\bar{\varepsilon}}^p}{\dot{\bar{\varepsilon}}_0}\right)\right][1 - \Theta^m] \quad (3)$$

Where Θ depends on the current temperature *T*, the melting temperature T_m and a reference temperature T_0 as:

$$\Theta = \frac{T - T_0}{T_m - T_0} \quad (4)$$

The parameters of the constitutive equation were identified for AA 2024-T351 by Teng and Wierzbicki [36] and are provided in Table 1 with other physical properties. The Taylor-Quinney coefficient which defines the percentage of plastic work converted into heat, was taken equal to $\beta = 0.9$ [38]. The initial temperature T_0 was set to 293 K and the melting temperature T_m for this alloy is 775 K. The density of the material is denoted by ρ and C_p is the specific heat at constant pressure.

In addition, the numerical model implemented in this work takes into account the temperature evolution assuming adiabatic heating. This is computed along the deformation process through the expression [39]:

$$\Delta T(\bar{\varepsilon}^p, \dot{\bar{\varepsilon}}^p, T) = \frac{\beta}{\rho C_p}\int_{\varepsilon^e}^{\bar{\varepsilon}^p} \bar{\sigma}(\bar{\varepsilon}^p, \dot{\bar{\varepsilon}}^p, T)\, d\bar{\varepsilon}^p \quad (5)$$

Elasticity		Thermoviscoplastic behaviour					
$E(GPa)$	$\nu(-)$	$A(MPa)$	$B(MPa)$	$n(-)$	$\dot{\bar{\varepsilon}}_0$ (s^{-1})	$C(-)$	$m(-)$
70	0.3	352	440	0.42	$3.3\ 10^{-4}$	0.0083	1.7
Other physical constants							
$\rho(kg/m^3)$	$\beta(-)$	$C_p(J/kg\ K)$	$T_0(K)$	$T_m(K)$			
2700	0.9	900	293	775			

Table 1: Properties of AA 2024-T351 and JC parameters [36].

3.2 SPH conversion criterion

The original mesh of the numerical model has been defined using Lagrangian elements. These elements are converted into SPH particles when a "flag variable" reaches a critical value. In this work, the equivalent plastic strain has been selected as the mechanical variable controlling the FEM-SPH conversion. The features of the model (initial, boundary conditions and contact interactions) are transferred appropriately when SPH particles are generated. The main advantage of the conversion approach over the SPH formulation is the reduction in the computational cost.

Therefore, a critical value of the equivalent plastic strain implies the conversion of the Lagrangian element into a sphere $\bar{\varepsilon}^{\mathrm{p}} \geq \bar{\varepsilon}^{\mathrm{p}}_{\mathrm{crit}}$. Once the conversion of the elements is reached, due to the nature

of the impact problem, the SPH particles overpass the boundaries of their action domain leading to failure. The boundaries of this action domain are defined by a characteristic length that, if is small enough, allows the assumption of considering the conversion criterion as the failure one. The critical equivalent plastic strain is then directly related to failure and was found to vary with the nose shape of the projectiles. This suggests a dependence of $\bar{\varepsilon}^{p}_{crit}$ on stress state. Then, the general form of this type of conversion strain can be expressed as Eq. (6):

$$\bar{\varepsilon}^{p}_{crit} = f(\eta) \tag{6}$$

Where η is the stress triaxiality defined by the ratio of the mean stress σ_m to the equivalent stress $\bar{\sigma}$. This conversion criterion model based on the level of failure strain is often used in dynamic problems [14-16]. According to several works [11, 36], the average value of the stress triaxiality can be slightly approximated just before the failure of the target for each projectile studied. Then, the triaxiality values have been determined from the components of the stress tensor in the elements of the failure zone prior to perforation.

The critical values listed in Table 2 were identified for AA 2024-T351 based on an optimization process for the whole range of impact velocities considered depending on the projectile shape. The numerical optimization process minimized the error on the residual velocity with experiments. Figure 8 shows a comparison between the critical strain values obtained in this work and the failure strain values in a recent work of the authors [29], presenting good agreement between both results. These results provide validity of failure strain values employed in the present work. In addition, the numerical model provides faithfully predictions of postmortem deflections of the plates with respect to experiments. It can be concluded then, that the material failure during the perforation process is governed by irreversible deformation mechanisms that depend on the triaxiality value associated to each projectile shape.

Projectile shape	Conical	Hemispherical	Blunt
$\bar{\varepsilon}^{p}_{crit}$	0.21	0.2	0.33

Table 2: Failure strain values used to simulate perforation depending on the projectile shape.

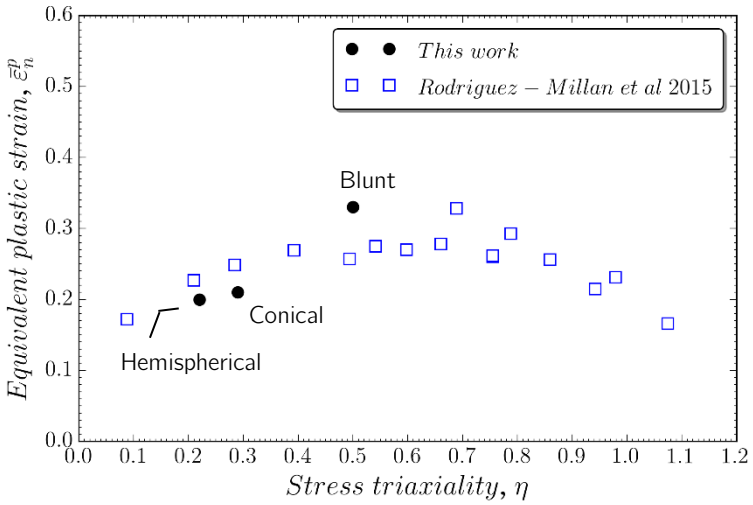

Fig. 8: Comparison of failure strain values between this work and data provided by Rodriguez-Millan and co-authors [29].

3.3 Mesh definition and boundary conditions used in numerical simulations

The numerical simulations of the impact problem were carried out using the commercial software ABAQUS 6.12/Explicit. The geometry of the targets and projectiles is the same as used in experiments. The mesh of the target plate included a total number of 264100 nodes and 242500 elements, see Figure 9. A total number of 12 elements were defined along the 4 mm thickness as recommended by Rodríguez-Martínez and co-authors [9]. The mesh was divided into three different zones as follows (see Figure 9):

- Zone A covers the contact region between the projectile and the target. The diameter of this region is similar to the diameter of the projectile. A mesh with 34900 eight-node brick hexahedral elements with one integration point, C3D8R in ABAQUS notation [23], was defined. These elements may be converted into SPH (PC3D elements).
- Zone B covers the transition region between the fine mesh zone (centre of target) and coarse mesh zone (boundary of target). The zone is defined by 44500 eight-node brick hexahedral elements with one integration point, C3D8R in ABAQUS notation [23]. These elements may also be converted into SPH (PC3D elements).
- Zone C covers the region that is located sufficiently far from the zone directly affected by the impact. This zone was meshed using 163150 hexahedral elements, C3D8R.

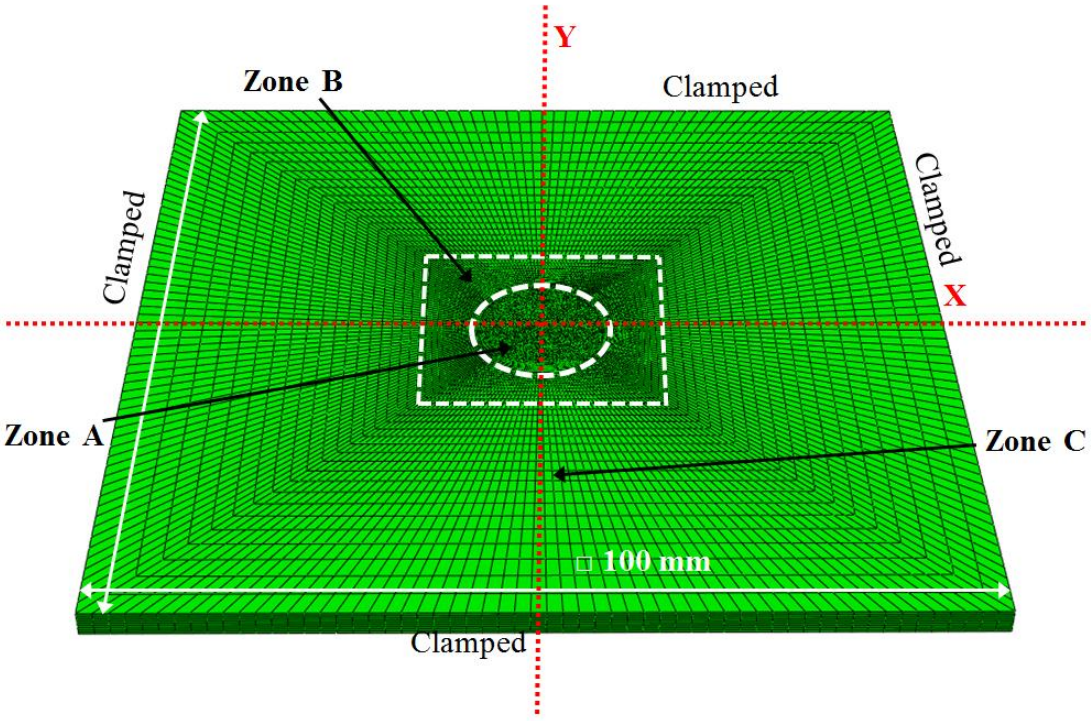

Fig. 9: Target mesh used in the numerical simulations.

The projectiles were modelled with a nominal mass and a maximum diameter of 30 g and 13mm respectively. The projectile was defined as an analytical rigid body since experimental tests revealed no plastic deformation on the projectile-surface after impact. This definition allows for reducing the computational cost required in the simulations. A friction coefficient equal to 0.1 was used to define the contact between the projectiles and the plate, as done by several other authors [2,6,9,21,32].

4. Numerical results and comparison with experimental data

4.1 Residual velocity

A comparison between experimental and numerical results in terms of residual versus impact velocities for different projectile nose shapes was carried out, see Figure 10. The use of a mesh density of 12 elements along the plate thickness was enough to simulate the perforation experiments accurately. The model provides a good correlation between numerical and experimental residual velocities depending on the impact velocity for the projectile shape configurations considered.

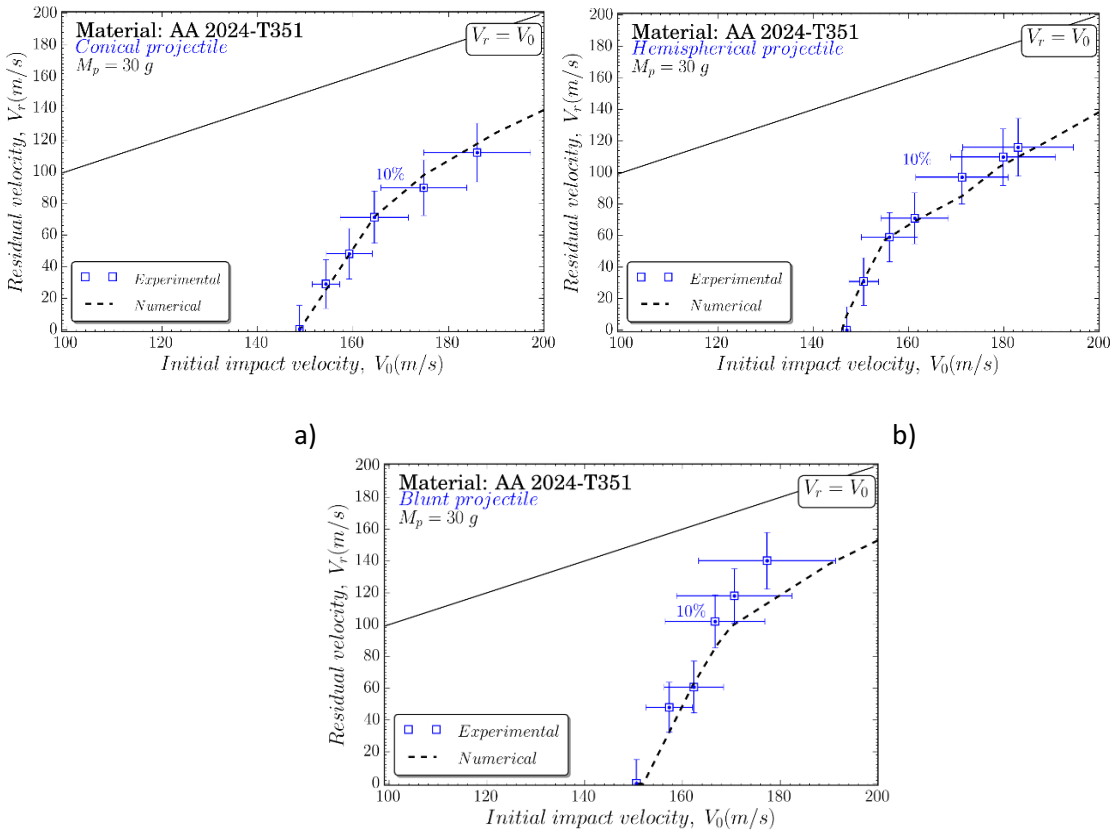

Fig. 10: Comparison of residual velocity V_r versus impact velocity V_0 between experiments and numerical simulations for: a) conical projectile; b) hemispherical projectile; and c) blunt projectile.

Once the model has been validated, it is used next to analyze the mechanisms behind the failure process.

4.2 Failure Mechanism

Figure 11 shows the perforation process for the three projectile configurations at three different stages. It can be observed that the largest density of SPH elements (converted from FEM) occurred when using the conical projectile nose.

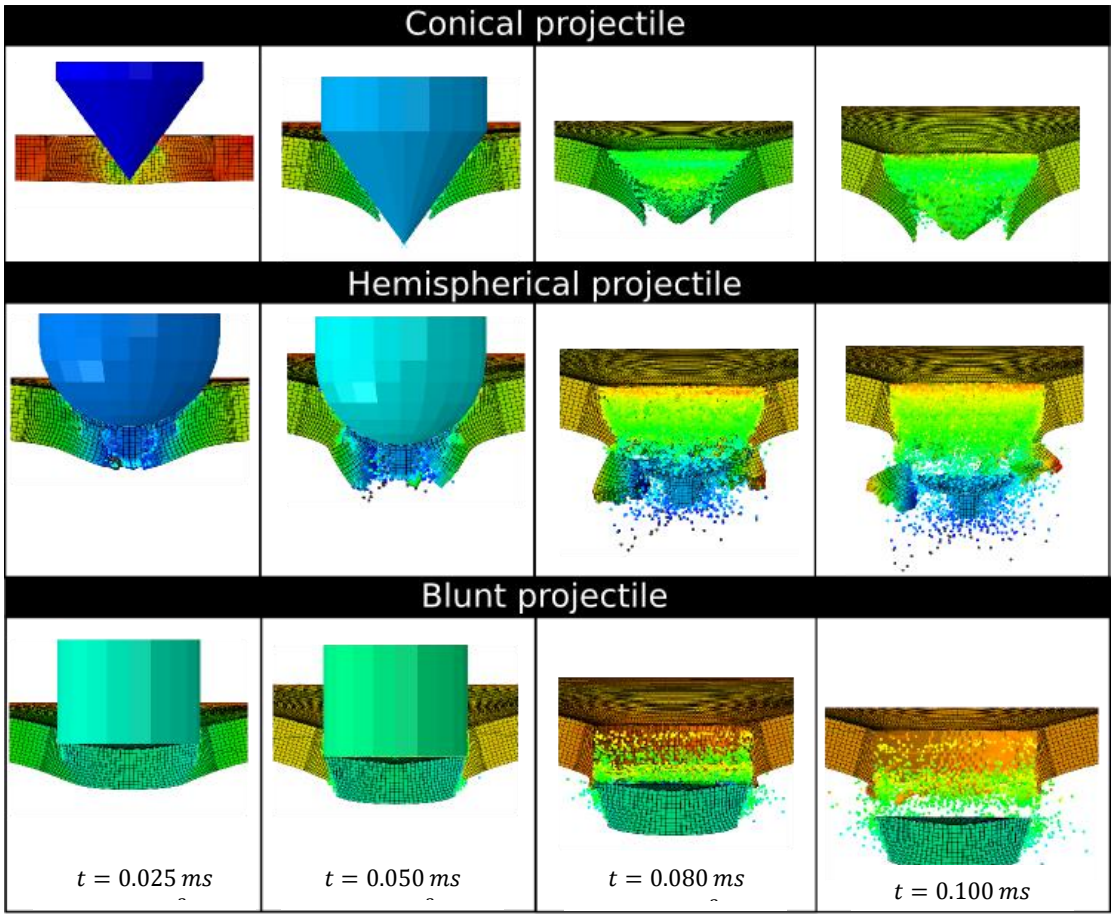

Fig. 11: Details of SPH element conversion and deformation behaviour of targets impacted at v=170 m/s by: a) conical; b) hemispherical; and c) blunt projectiles. (*For the sake of clarify, the projectiles are not displayed at t=0.080 and t=0.100 ms*)

Different failure modes have been observed during the perforation tests. Figure 12 presents a comparison between experiments and numerical simulations in terms of permanent plate bending for two impact velocities: 150 m/s and 180 m/s. The y-axis corresponds to the normalized displacement of the impacted plates w/t (where w is the out-of-plane displacement and t is the target thickness); and the x-axis represents the normalized target length. The numerical model provides better predictions for impact velocities above the ballistic limit. The following general observations were drawn from this analysis.

- For all projectile configurations, the deflection is maximum at velocities close to the ballistic limit. This behaviour is in agreement with the observed in other aluminium alloys [12].
- In the case of the blunt projectile configuration, the model predictions of the plate deflection are better than for the other two configurations. This can be explained by the predominance of the global mechanism -bending- on the deformation process.

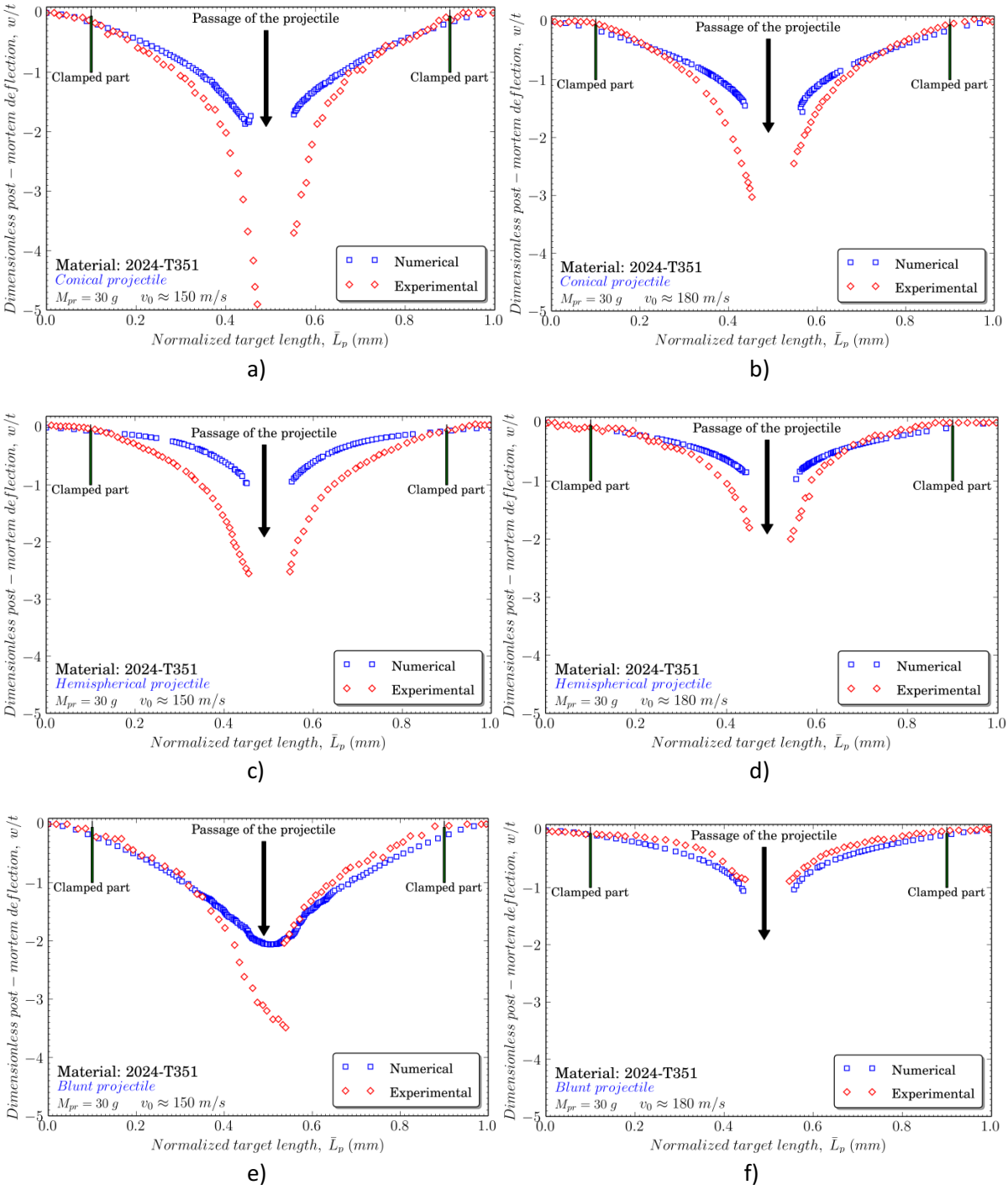

Fig. 12: Dimensionless post-mortem deflection of the plates as a function of the normalized target length for: (a) conical nose at $V_0 \sim 150$ m/s; (b) conical nose at $V_0 \sim 180$ m/s ; (c) hemispherical nose at $V_0 \sim 150$ m/s; (d) hemispherical nose at $V_0 \sim 180$ m/s; (e) blunt nose at $V_0 \sim 150$ m/s; and (f) blunt nose at $V_0 \sim 180$ m/s.

4.3 Energy absorption capacity

The total energy absorbed can be understood as the contribution of global and local deformations contributions. The present numerical modelling is necessary to develop a careful analysis of the energy absorbed by the plate within the impact velocity range considered. Thus, the target was modelled as

a local part (zone A in Figure 9) and a global part (zone B and C in Figure 9) with identical material properties. This allows for studying global versus local energy absorptions during penetration. In this work, the local energy absorption is associated with local failure mechanisms (shear, petalling and plugging); and the global energy absorption is associated with deformation mechanism (general bending).

The sensitivity of global (E_G), local (E_L), deformation (E_D) and absorption (E_A) energies to impact velocity is assessed for all projectiles, see Figure 13. The energy absorbed is defined as the difference between the initial and final kinetic energy, Eq. (2). The global energy (E_G) is the sum of internal energy of the elements of zones B and C (Figure 9), while the local energy (E_L) is the same sum but for the elements of the local region (zone A in Figure 9). The deformation energy $E_D = E_G + E_L$ is defined by the sum of local and global energies.

For all nose shapes, it is remarkable that the local energy slightly increases while the global energy decreases with impact velocity. These results suggest that impact velocity is the variable that governs the main deformation mechanisms. As this variable increases, a progressive change can be observed from a global mechanical resistance to deformation associated with the overall response of the structure as a whole, to a local mechanical resistance associated with local deformation and failure mechanisms such as shearing, plugging or petalling. In addition, the global to local energy transition has been found to depend on the projectile nose shape and, therefore, on the triaxiality and failure mechanisms associated. For the case of blunt projectile, the thickness of plug is similar to the plate one. According to previous work [21], the adiabatic shear bands (ASB) velocity is faster than the initial impact velocity, inducing a failure by ASB propagation and obtaining local energy higher than global energy as demonstrated in Figure 13. In this regard, plugging mechanism associated with type of projectile shows the sharpest energy transition. Moreover, the evolution of these energies revealed 15% to 20% differences between absorption energy and deformation energy for the three projectile configurations. Although some cracks propagate reaching zone B, the energy consumed in this region due to such effects can be neglected with respect to the energy associated to local energy in zone A. This issue has been analysed by varying the relative dimensions of both zones in order to keep the local cracks into zone A. The dimensions used in this work are consistent for the different configurations used in terms of energy evaluation.

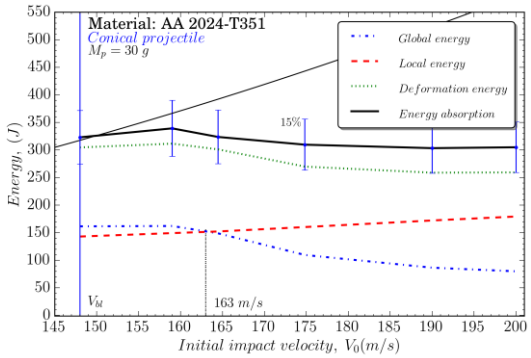

a)

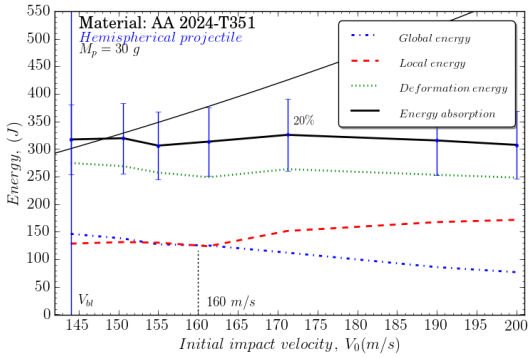

b)

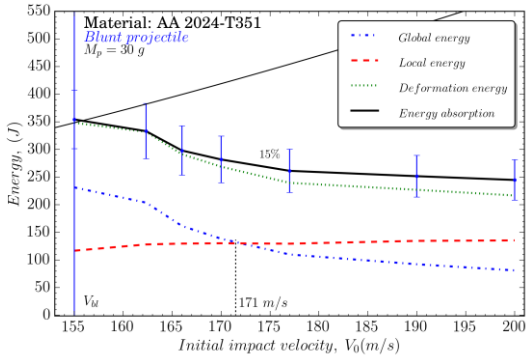

c)

Fig. 13: Numerical prediction of the evolution of global, local, total and absorption energies versus impact velocity for: a) conical; b) hemispherical; and c) blunt projectiles.

It can be also observed from Figure 13, that there is a velocity at which the global energy is equal to the local energy; defined here as *neutral velocity.* For the sake of clarity, a bar chart comparison between ballistic limit and neutral velocity for the three projectiles is presented in Figure 14. The ballistic limit and neutral velocity seems to be dependent on projectile shape-nose. In this regards, blunt projectile exhibits higher ballistic limit and neutral velocity than conical and hemispherical projectiles.

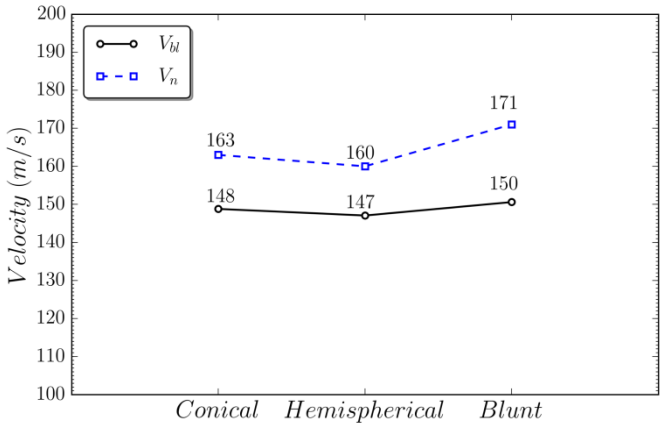

Fig. 14: Differences between ballistic limit and neutral velocity for conical, hemispherical and blunt projectile.

The observations mentioned above, reinforce the idea that the impact energy is absorbed by a combination of local and global deformation mechanisms. It is also important to emphasize the need of developing reliable numerical models in order to obtain accurate predictions of the mechanical behaviour of materials under impact loading.

5. Conclusions

In this paper an experimental and numerical analysis of the influence of projectile geometry on the ballistic performance of 2024-T351 aluminium alloy is presented. Projectiles with conical, hemispherical and blunt nose shapes were considered. Residual velocities, failure mechanisms and energy absorption during and after impact were investigated at velocities up to 200 m/s. The conversion FEM-SPH method was used in this study providing accurate predictions of the mechanical behaviour of AA 2024-T351 under impact loading. The simulations allowed for the understanding of impact phenomena and deformation energy distribution along the aluminium plates. No significant difference in the ballistic resistance was observed between three nose shape projectiles considered. However, a relevant variation in residual velocity was noted as the impact velocity increases. The amount of kinetic energy converted into global and local energy strongly depends on the nose-shape of the projectile as revealed by numerical simulations. At low impact velocities, the global energy was higher for blunt nose shape while at high impact velocities local energy was more significant for hemispherical and conical nose shapes.

In conclusion, the stress state has been demonstrated to be a key variable in determining the failure mechanisms and the FEM-SPH method has been found to be a valid way to analyze this influence in impacts events.

Acknowledgements

The researchers are indebted to the Ministerio de Economía y Competitividad de España (Project DPI2014-57989-P) for the financial support which permitted to conduct part of this work.

Appendix A. Quasi-static tests on 2024-T351 aluminium alloy

In order to verify the material used in this work and prior to identify the material parameters for its mechanical modelling, quasi-static compression tests were performed. The results obtained from such tests are in good agreement with the ones reported by other authors for this material [41-43], see Fig A.1.

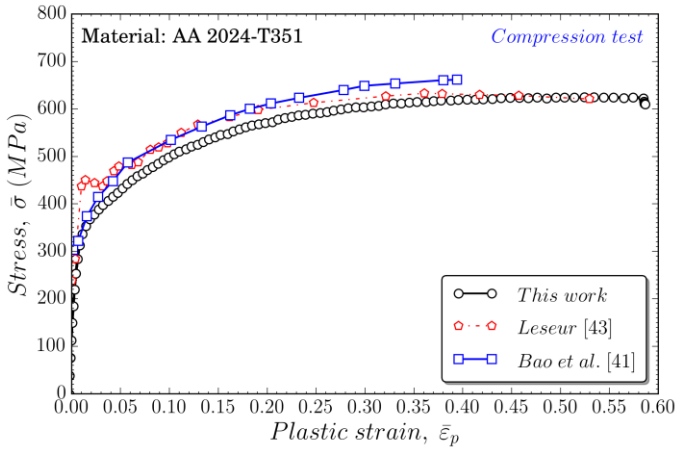

Fig. A.1: Quasi-static compression test for AA 2024-T351. Comparison of the stress-strain curve obtained for the material used in this work with published data.

In addition, the material parameters identified for the JC model used in this work have been compared with the ones provided by other authors, finding again a good agreement between them:

A (MPa)			B (MPa)			n (-)		
Our test	Bao et al. [41]	Error (%)	Our test	Bao et al. [41]	Error (%)	Our test	Bao et al. [41]	Error (%)
329.3	352	6.44	431.7	440	1.88	0.36	0.42	14.2

Fig. A.2: Quasi-static compression test for AA 2024-T351. Comparison of the stress-strain curve obtained for the material used in this work with published data.

References

[1] National High way Traffic Safety Administration-NHTSA (2014), Early Estimate of Motor Vehicle Traffic. Fatalities for the First Nine Months of 2013. Technical Report, U.S. Department of Transportation.

[2] Børvik T, Langseth M, Hopperstad OSS, Malo KA, Berstad T (2002) Perforation of 12 mm thick steel plates by 20 mm diameter projectiles with flat, hemispherical and conical noses Part II: numerical simulations. Int. J. Impact Eng. 27:37–64.

[3] Børvik T, Hopperstad OS, Langseth M, Malo KA (2003) Effect of target thickness in blunt projectile penetration of Weldox 460 E steel plates. Int. J. Impact Eng. 28(4): 413–464.

[4] Børvik T, Clausen AH, Hopperstad OS, Langseth M (2004) Perforation of AA5083-H116 aluminium plates with conical-nose steel projectiles—experimental study. Int. J. Impact Eng. 30(4):367–384.

[5] Gupta NK, Madhu V (1992) Normal and oblique impact of kinectic energy projectile on mild steel plates, Int. J. Impact Eng. 12(3): 333–343.

[6] Gupta NK, Iqbal MA, Sekhon GS (2006) Experimental and numerical studies on the behavior of thin aluminum plates subjected to impact by blunt- and hemispherical-nosed projectiles, Int. J. Impact Eng. 32(12):1921–1944.

493 [7] Senthil K, Iqbal MA, Arindam B, Mittal R, Gupta NK (2017) Ballistic resistance of 2024 aluminium
494 plates against hemispherical, sphere and blunt nose projectiles, Thin-Walled Structures, Available
495 online 3 March 2017.
496 [8] Dey S, Børvik T, Hopperstad OS, Leinum JR, Langseth M (2004) The effect of target strength on the
497 perforation of steel plates using three different projectile nose shapes. Int. J. Impact Eng. 30(8-9):
498 1005–1038.
499 [9] Rodríguez-Martínez JA, Rusinek A, Pesci R, Zaera R (2013) Experimental and numerical analysis of
500 the martensitic transformation in AISI 304 steel sheets subjected to perforation by conical and
501 hemispherical projectiles. Int. J.Solids Struct. 50(2):339–351.
502 [10] Kpenyigba KM, Jankowiak T, Rusinek A, Pesci R (2013) Influence of projectile shape on dynamic
503 behavior of steel sheet subjected to impact and perforation, Thin Wall. Struct. 65:93-104.
504 [11] Kpenyigba KM, Jankowiak T, Rusinek A, Pesci R, Wang B (2015) Effect of projectile nose shape on
505 ballistic resistance of interstitial-free steel sheets, Int. J. Impact Eng. 79:83–94.
506 [12] Rodríguez-Millán M, Vaz-Romero A, Rusinek A, Rodríguez-Martínez JA, Arias A (2014)
507 Experimental Study on the Perforation Process of 5754-H111 and 6082-T6 Aluminium Plates Subjected
508 to Normal Impact by Conical, Hemispherical and Blunt Projectiles, Exp. Mech. 54(5):729–742.
509 [13] Manes A, Lumassi D, Giudici L, Giglio M (2013) An experimental–numerical investigation on
510 aluminium tubes subjected to ballistic impact with soft core 7.62 ball projectiles, Thin Wall Struct, 73:
511 68-80
512 [14] Mars J, Wali M, Jarraya A, Dammak F, Dhiab A (2015) Finite element implementation of an
513 orthotropic plasticity model for sheet metal in low velocity impact simulations, Thin Wall Struct, 89:93-
514 100.
515 [15] Dey S, Børvik T, Teng X, Wierzbicki T, Hopperstad OS (2007) On the ballistic resistance of double-
516 layered steel plates: An experimental and numerical investigation, Int. J. Solids Struct 44(20): 6701–
517 6723.
518 [16] Rusinek A, Rodríguez-Martínez JA, Zaera R, Klepaczko JR, Arias A, Sauvelet C (2009) Experimental
519 and numerical study on the perforation process of mild steel sheets subjected to perpendicular impact
520 by hemispherical projectiles, Int. J. Impact Eng. 36(4):565–587.
521 [17] Iqbal MA, Gupta NK (2011) Ballistic Limit of Single and Layered Aluminium Plates, Strain. An Int.
522 Exp. Mech. 47:205–219.
523 [18] Jankowiak T, Rusinek A, Wood P (2013) A numerical analysis of the dynamic behaviour of sheet
524 steel perforated by a conical projectile under ballistic conditions, Finite Elem. Anal. Des. 65: 39–49.
525 [19] Takaffoli M, Papini M (2009) Finite element analysis of single impacts of angular particles on
526 ductile targets, Wear 267:144–151.
527 [20] Campbell J, Vignjevic R (1997) Development of Lagrangian hydrocode modelling for debris impact
528 damage prediction, Int. J. Impact Eng. 20:143–152.
529 [21] Arias A, Rodríguez-Martínez JA, Rusinek A (2008) Numerical simulations of impact behaviour of
530 thin steel plates subjected to cylindrical, conical and hemispherical non-deformable projectiles, Eng.
531 Fract. Mech. 75:1635–1656.
532 [22] Rusinek A, Rodríguez-Martínez JA, Arias A, Klepaczko JRR, López-Puente J (2008) Influence of
533 conical projectile diameter on perpendicular impact of thin steel plate. Eng. Fract. Mech. 75 2946–
534 2967.
535 [23] Dassault Systèmes (2012) Abaqus v6.12 Documentation- ABAQUS analysis user's manual. ABAQUS
536 Inc; 6.12.

[24] Takaffoli M, Papini M (2012) Material deformation and removal due to single particle impacts on ductile materials using smoothed particle hydrodynamics, Wear 274-275: 50–59.
[25] Johnson GR, Stryk RA, Beissel SR (1996) SPH for high velocity impact computations. Comp. Method. Appl. M. 139:347–73.
[26] Zhang Z, Qiang H, Gao W (2011) Coupling of smoothed particle hydrodynamics and finite element method for impact dynamics simulation, Eng. Struct. 33 255–264.
[27] Johnson GR (1994) Linking of Lagrangian particle methods to standard finite element methods for high velocity impact computations, Nucl. Eng. Des. 150:265–74.
[28] Johnson GR, Beissel SR, Gerlach C (2013) A Combined Particle-element Method for High-velocity Impact Computations. Procedia Eng. 58:269–278.
[29] Rodríguez-Millán M, Vaz-Romero Á, Arias, Á (2015) Failure behavior of 2024-T3 aluminum under tension-torsion conditions. J. Mech Sci. Technol. 29(11): 4657-4663.
[30] Rodríguez-Martínez JA, Rusinek A, Chevrier P, Bernier R, Arias A (2010) Temperature measurements on ES steel sheets subjected to perforation by hemispherical projectiles, Int. J. Impact Eng. 37: 828–841.
[31] Recht RF, Ipson TW (1963) Ballistic Perforation Dynamics. Journal of Applied Mechanics.
[32] Rodríguez-Martínez JA, Rusinek A, Arias (2010) A Thermo-viscoplastic behaviour of 2024 T3 aluminium sheets subjected to low velocity perforation at different temperatures. Thin Wall. Struct. 47:1268–1284.
[33] Atkins AG, Khan MA, Liu JH (2013) Experimental and numerical analysis of the martensitic transformation in AISI 304 steel sheets subjected to perforation by conical and hemispherical projectiles. Int. J. Solid. Struct. 50 339–351.
[34] Xue L (2007) Damage accumulation and fracture initiation in uncracked ductile solids subject to triaxial loading, Int J Solids Struct 44 (16): 5163-5181.
[35] Steglich D, Brocks W, Heerens J, Pardoen T (2008) Anisotropic ductile fracture of Al 2024 alloys, Eng Fracture Mech 75 (12):3692-3706.
[36] Teng X, Wierzbicki T (2005) Numerical study on crack propagation in high velocity perforation, Comput. Struct. 83:989-1004.
[37] Johnson GR, Cook WH (1983) A constitutive model and data for metals subjected to large strains high strain rates and high temperatures. In: Proceedings of the seventh international symposium on ballistics.
[38] Garcia-Gonzalez D, Rodríguez-Millan M, Vaz-Romero A, Arias A (2015) High impact velocity on multi-layered composite of polyether ether ketone and aluminium. Compos. Interface http://dx.doi.org/10.1080/09276440.2015.1051421
[39] Garcia-Gonzalez D, Rusinek A, Jankowiak T, Arias A (2015) Mechanical impact behavior of polyether-ether-ketone (PEEK). Compos. Struct. 124: 88-99.
[40] W.Z. Zhong, I.A. Mbarek, A. Rusinek, R. Bernier, T. Jankowiak, G. Sutter (2016) Development of an experimental set-up for dynamic force measurements during impact and perforation, coupling to numerical simulations, Int. J. Impact Eng., 91:102–115.
[41] Y. Bao, T. Wierzbicki (2003) Prediction of Ductile Crack Formation in Uncracked Bodies. Massachussetts Institute of Technology.
[42] X. Teng, T. Wierzbicki (2006) Evaluation of six fracture models in high velocity perforation. Eng Fract Mech;73:1653–78.
[43] D.R.Lesuer (2000) Experimental investigations of material models for Ti-6Al-4V titanium and 2024-T3 aluminum. Lawrence Livermore National Laboratory. Report No.DOT/FAA/AR-00/25., http://actlibrary.tc.faa.gov.